Additive Manufacturing 71 (2023) 103579

Contents lists available at ScienceDirect

Additive Manufacturing

journal homepage: www.elsevier.com/locate/addma

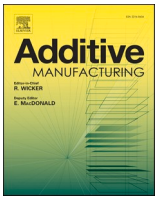

In situ correlative observation of humping-induced cracking in directed energy deposition of nickel-based superalloys

Tristan G. Fleming [a,*], David Tien Rees [b,c], Sebastian Marussi [b,c], Thomas Connolley [d], Robert C. Atwood [c,d], Martyn A. Jones [e], James M. Fraser [a,*], Chu Lun Alex Leung [b,c], Peter D. Lee [b,c,**]

[a] Department of Physics, Engineering Physics & Astronomy, Queen's University, Kingston, Ontario K7L 3N6, Canada
[b] Department of Mechanical Engineering, University College London, WC1E 7JE, UK
[c] Research Complex at Harwell, Rutherford Appleton Laboratory, Harwell, Didcot OX11 0FA, UK
[d] Diamond Light Source, Diamond House, Harwell Campus, Chilton, Didcot, OX11 0DE, UK
[e] Rolls-Royce plc, PO Box 31, Derby DE24 8BJ, UK

ARTICLE INFO

Keywords:
Inline coherent imaging
Directed energy deposition
Synchrotron X-ray imaging
Humping and cracking defects
In situ monitoring

ABSTRACT

Directed energy deposition (DED) is a promising additive manufacturing technique for repair; however, DED is prone to surface waviness (humping) in thin-walled sections, which increases residual stresses and crack susceptibility, and lowers fatigue performance. Currently, the crack formation mechanism in DED is not well understood due to a lack of operando monitoring methods with high spatiotemporal resolution. Here, we use inline coherent imaging (ICI) to optically monitor surface topology and detect cracking in situ, coupled with synchrotron X-ray imaging for observing sub-surface crack healing and growth. For the first time, ICI was aligned off-axis (24° relative to laser), enabling integration into a DED machine with no alterations to the laser delivery optics. We achieved accurate registration laterally (<10 μm) and in depth (<3 μm) between ICI measurements and the laser beam position using a single-element MEMS scanner and a custom calibration plate. ICI surface topology is verified with corresponding radiographs (correlation >0.93), directly tracking surface roughness and waviness. We intentionally seed humping into thin-wall builds of nickel super-alloy CM247LC, locally inducing cracking in surface valleys. Crack openings as small as 7 μm were observed in situ using ICI, including sub-surface signal. By quantifying both humping and cracking, we demonstrate that ICI is a viable tool for in situ crack detection.

1. Introduction

Additive manufacturing (AM) promises to allow the direct transfer of a 3D design to final part production with almost unlimited design freedom. Of the seven categories of AM identified by ASTM, two of the most commonly used for metals are powder bed fusion (PBF) and directed energy deposition (DED) [1]. Although DED was invented first [2], its adoption currently lags PBF [3], which has begun to deliver as promised and is now regularly used for small/medium batch, complex components [4]. This is despite DED's clear differentiating factors: large build volumes (meters vs. 100 s of cm), the possibility for functionally graded materials (FGMs), and the repair of existing high-value components [5,6]. These advantages have established DED for specific components/applications, but in limited number and often for conventional and large geometries. To extend these advantages to more complex components, the role of the underlying part geometry needs to be better understood to improve the repeatability and adaptability of the DED process. This is especially true for complex, thin-walled geometries, which are prone to distortion and residual stress build-up during DED. In addition, many nickel super-alloys (MAR-M247, CM-247) are classified as non-weldable [7] and are susceptible to cracking under high thermal and residual stresses typical of DED [8].

Thin-wall structures are commonly found in the aerospace, automotive and energy industries, e.g. wing ribs and spars, turbine blades, vanes and casings [9]. Their use is increasing as part of lightweighting [10,11]. However, due to their low rigidity, thin-walled structures tend

* Corresponding authors.
** Corresponding author at: Department of Mechanical Engineering, University College London, WC1E 7JE, UK.
E-mail addresses: tristan.fleming@queensu.ca (T.G. Fleming), jf9@queensu.ca (J.M. Fraser), peter.lee@ucl.ac.uk (P.D. Lee).

https://doi.org/10.1016/j.addma.2023.103579
Received 19 February 2023; Received in revised form 9 April 2023; Accepted 24 April 2023
Available online 26 April 2023

to vibrate and deflect during traditional manufacturing like CNC milling. This can degrade dimensional accuracy and surface finish, increase scrap rates, and may damage the milling machine [12,13]. Vibration and deflection also scale with the required cutting force, making them particularly problematic for titanium and nickel alloys. Furthermore, milling of thin-walled structures is wasteful. Large monolithic components can require the removal of up to 95% of the raw material, severely increasing buy-to-fly ratios to greater than 10:1 [14]. With these problems in mind, DED of thin-walled structures has become an active area of research, with particular attention on repair and remanufacture applications [15–17]. Unfortunately, the large and non-uniform thermal gradients inherent to the DED process [18] have proven difficult to overcome, leading to persistently poor dimensional accuracy and surface finish, and high residual stresses [19,20]. The lack of consideration for interactions between process parameters is one reason for these persistent defects, termed "synchronistic behaviour" by Izadi *et al.* [21].

In DED, the melt pool size is directly linked to build height through the powder catchment efficiency [22] (just considering geometric factors: $\dot{m} \propto A_{int}/A_p$, where $\dot{m}$ is the mass build rate, A_{int} is the area at the track surface over which the incoming powder stream interacts with melt and A_p is the total area of the powder stream). More powder particles are "caught" by a larger melt pool. Melt pool size is dictated by energy density [23] as well as part geometry. As a result of these interactions, there are several sources of surface roughness and waviness in DED. Without a "flying" start, the limited acceleration of a traverse stage or robot arm means energy density is higher at the start of a layer. This explains why the edges of a DED part are sometimes raised and "bulged". For thin-walled structures, with one less axis for heat to conduct away from the melt pool, heat build-up can increase melt pool size both intra- and inter-layer. This leads to non-uniform layer thickness and width [24]. Another common defect in DED is inconsistent powder flow rate, caused by nozzle clogs, improper carrier gas flow and poor powder quality (satellites, clumping). Variations in melt pool size can be coupled with variations in powder flow to generate surface waviness or "humping" [25]. Over multiple layers, humping can "runaway" or accumulate due to the variations in nozzle working distance between the raised peaks and lowered valleys. If valleys fall below the laser and/or powder jet focus, even less material will be deposited in these areas, lowering them further, referred to as passive instability [26]. In addition to a clear geometric defect, humping also further increases crack susceptibility in DED-built material.

Cracking can significantly reduce fatigue life and creep performance [27]. High thermal gradients induce very high residual stress, which, coupled with inter-dendritic liquid remaining present to lower temperatures due to high cooling rates, means DED is susceptible to crack formation [28]. This is exacerbated in nickel superalloys where multiple phases/precipitates (γ, γ', γ'', Laves and δ) can form due to elemental segregation, independently influencing the deformation states at the microscale [29]. If humping occurs, the resulting residual stress distribution further increases crack susceptibility. The peaks adjacent to a valley, which will be relatively cold when the laser is positioned over the valley, further restrict thermal expansion and contraction of the melt pool/HAZ in the valley. For thin walls, the layer and wall will also be thinner in valleys than peaks, where lower peak temperatures reduce outward and transverse Marangoni convection leading to smaller melt pools, concentrating thermal stresses in this region. This is emblematic of the general effect of underlying part geometry on thermal and residual stresses [30].

Several research groups have implemented adaptive process control of DED to improve geometric accuracy [31], highlighting the need for process monitoring. Numerous different sensors have been used to monitor the DED process [32–34]. Most common are temperature sensors (visible or near-infrared thermal cameras [35], pyrometers [36]) for measuring melt pool dimensions, and geometry sensors (laser profilometers [37,38], structured light systems [39], and stereo-vision systems [40–42]) for measuring nozzle working distance and track height/distortion. Recently, Donadello *et al.* developed a coaxial laser triangulation system for relatively slow (<100 Hz) but inexpensive and robust measurements of track height, with an axial and transverse resolution of 200 and 270 μm, respectively [43]. Additionally, Kogel-Hollacher *et al.* [44] integrated a low-coherence interferometry system into a DED system using a similar technique as described in this paper. They achieved some control of track height but only provided post-deposition images of thin-wall builds with/without control.

Though these systems have provided important insights into the DED process, none correlated temperature or geometry signatures with cracking. To the authors' knowledge, this has only been achieved in DED by monitoring acoustic emissions (AE) [45,46]. Gaja *et al.* [47] characterized AE signatures for pore formation and cracking during DED using a logistic regression/artificial neural network model trained by manually identifying defects ex situ with optical microscopy. Hauser *et al.* [48] delineated the sources of AE during DED including melting, solidification and collision of powder particles and linked them to geometrical fluctuations, oxidation and sputtering process defects. While this work is promising, cracking signatures were not recorded. In both cases, more work is needed to integrate AE monitoring into a harsher and noisier industrial environment.

In this paper, a low-coherence interferometric imaging technique called inline coherent imaging (ICI) is integrated into a DED system to in situ and operando monitor track morphology at micron-resolution (axial and transverse resolutions of 6 μm and 35 μm) and high-speeds (200 kHz). This exploits the inherent robustness of ICI to high-power laser light and process emission as demonstrated in numerous other laser material processing applications [49]. Here, we demonstrate that ICI can capture surface roughness, including sintered powder particles on the track surface, and waviness or humping, a key precursor to cracking. For the first time, the morphology signature of crack openings at the track surface is recorded in situ with ICI. To understand these signatures and link the timing and position of the measured crack openings with sub-surface cracking phenomena, ICI is combined with simultaneous synchrotron X-ray radiography. Synchrotron X-ray radiography has been recently used to observe cracking phenomena in high-power laser welding and PBF of aluminum alloy 6061, elucidating crack formation and growth rate, pore-crack interactions, as well as crack healing by melt backfilling in Al6061 [50,51]. Particularly relevant to the work presented here, Tabasi *et al.* observed crack formation and growth over multi-layer PBF of nickel superalloy CM247LC and were able to conclusively distinguish between solidification and liquation cracking mechanisms using post-mortem SEM analysis and numerical simulations [52]. However, the mechanisms at play during DED have still yet to be observed operando in industry-relevant conditions.

2. Materials and methods

The experimental set-up consisted of: a bespoke DED system, the Blown Powder Additive Manufacturing Process Replicator (BAMPRII, second generation, detailed in [53]); synchrotron X-ray beamline, I12 Joint Engineering, Environmental, and Processing (JEEP) at the Diamond Light Source, used to capture in situ and operando radiographs; and an interferometric, inline coherent imaging (ICI) system for simultaneous and high-speed, in situ and operando morphology measurements.

2.1. Directed energy deposition

BAMPRII was used to build thin-wall pre-builds before the beamtime and deposit further layers during the beamtime (see Appendix A for build strategy). BAMPRII is designed for synchrotron X-ray imaging of DED while replicating industrial conditions, featuring: an inert environmental chamber (here maintained <100 ppm O_2), an industrial powder feeder and nozzle (Oerlikon Metco TWIN-10-C), a 200 W,

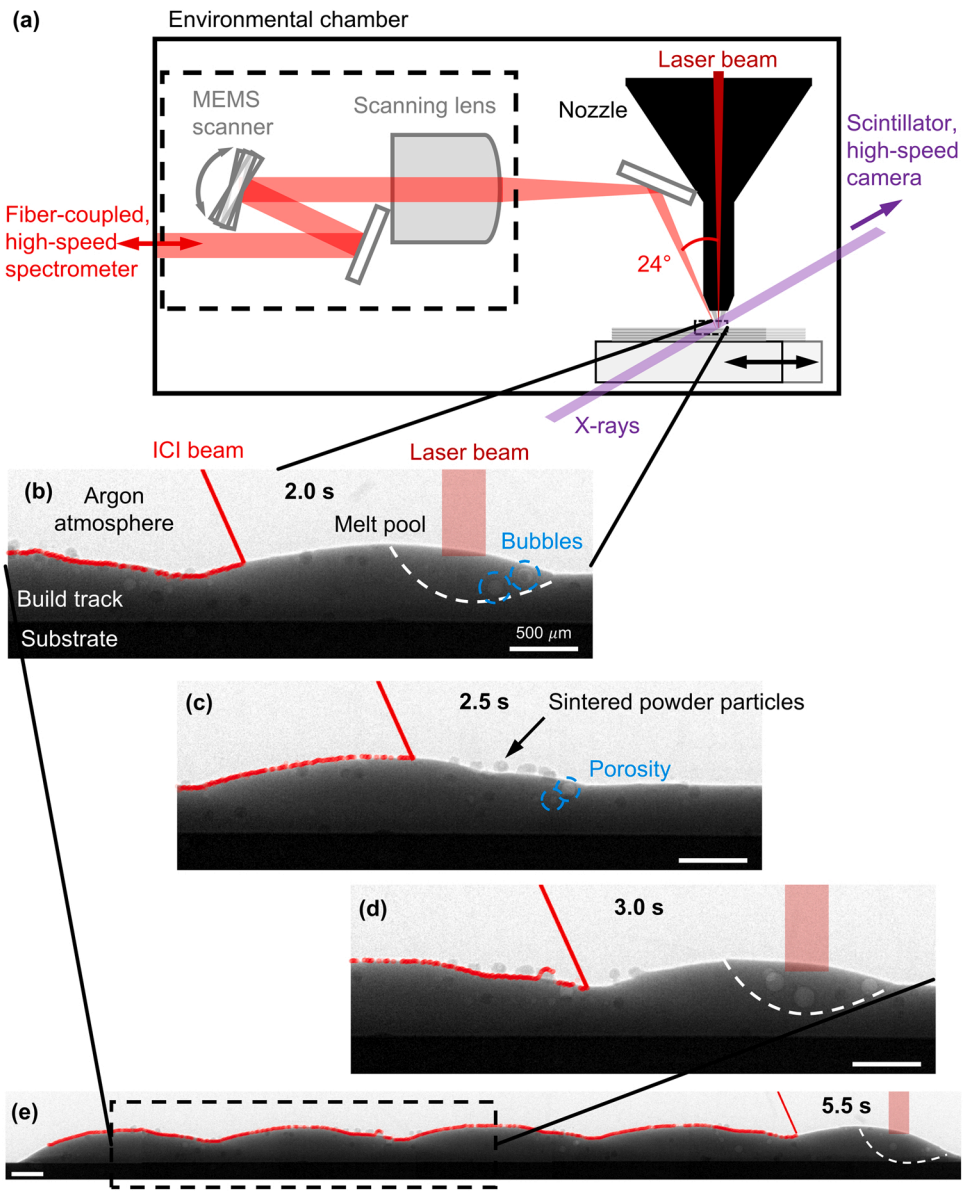

Fig. 1. Simultaneous operando X-ray and inline coherent imaging of the DED-AM process. (a) Schematic of the Blown Powder Additive Manufacturing Process Replicator (BAMPRII) environmental chamber, including integrated scanning and focusing optics for inline coherent imaging (ICI). (b-e) Example time-resolved radiographs from an "on-off" build track overlaid with surface morphology measured using ICI (red dots). ICI captures features only within a narrow cross section. See Supplementary Movie 1 for full time-resolved ICI and X-ray signatures. Total track length is 14 mm, laser switched on for 800 ms (2 mm) then off for 400 ms (1 mm), four times. Process parameters: laser power 200 W, traverse speed 2.5 mm/s, powder feedrate 2.15 g/min, substrate material IN718, powder material CM247LC.

1070 nm Ytterbium-doped fiber laser delivered coaxial to the powder nozzle (SPI Lasers, Ltd., CW, Gaussian distribution, $1/e^2$ beam diameter of 320 μm, Rayleigh range of 63 mm), and a three-axis motion stage for sample positioning and motion, and X-ray imaging with a Lagrangian frame of reference.

Two different Ni-superalloy powders were used for this study, CM247LC (Carpenter Powder Products Inc.) and Inconel 718 (IN718) (Rolls-Royce plc). The latter was mixed with 40 wt% tungsten carbide (WC) particles (Oerlikon Metco 50050A) for a separate study on protective coatings. In situ imaging results are included from five different thin-wall builds. Due to its higher susceptibility, CM247LC was used in builds investigating cracking. IN718 was used in an initial set of builds to verify the imaging capabilities of the ICI system. The powder morphology and size distribution were measured using scanning electron microscopy (SEM). Example SEM images are shown in Appendix A, Figure A1. Dv10, Dv50, and Dv90 values were calculated by segmenting the particles in the SEM images using the Otsu method and watershed algorithm in Matlab R2021b and found to be 50.6 μm, 85.7 μm and 103.9 μm for CM247LC and 42.8 μm, 55.1 μm and 79.1 μm for IN718 + WC [54]. All substrates were IN718, ~58 mm x 20 mm x 1.6 mm (EDM cut, Hardmetal Technology Ltd), sanded down to 1000 grit and then cleaned with isopropanol before processing. Any effect of the difference in alloying content between substrate and deposit when using CM247LC powder is expected to be isolated to initial layers and is avoided with the build geometry used in this study (Appendix A). The disc rotation speed of the powder feeder and carrier gas flow rate (Ar) were held constant at 20 rpm and 6 L/min, respectively, producing a measured mass flow rate of 2.1 ± 0.1 g/min for CM247LC and 3.4 ± 0.1 g/min for IN718 + WC.

2.2. Synchrotron X-ray imaging

The X-ray beam energy was set to 70 keV for CM247LC and 68 keV for IN718 +WC, the slight adjustment to avoid the K-absorption edge of tungsten. The imaging system consisted of a 700 μm thick LuAg:Ce scintillator, a custom optical module (module 3) that set the pixel resolution and maximum field of view to 6.67 μm x 6.67 μm/pixel and 8.5 mm x 5.3 mm, and a MIRO 310M camera (Vision Research, Inc). Frame rate was held constant at 1000 fps with maximum ~1 ms exposure time. Before depositing layers on each build, two sets of dark and flat field images were collected, with the same number of frames captured for each layer of the build, one for each of the two traverse

directions used in the bidirectional build strategy. This was done by executing the same stage motion patterns but without the substrate in the X-ray FOV and without firing the laser, with (flat field) and without (dark field) opening the beamline shutter. All the acquired radiographs were then processed in Matlab R2021b by applying a flat field correction according to: $FFC(n) = (I_0(n) - Flat(n))/(Flat(n) - Dark(n))$, where n denotes the frame number, *FFC* is the flat field corrected image, I_0 is the corresponding raw image, *Flat* is the corresponding flat field image and *Dark* is the corresponding dark field image. The function "imgaussfilt" built into the Matlab Image Processing Toolbox was then used to Gaussian filter each radiograph, with a standard deviation of 0.5 pixels [55]. For radiographs with cracking, two additional image processing steps were applied to better resolve the cracks: (1) VBM4D denoising algorithm with automatic noise estimation [56], and (2) histogram stretching (saturating top and bottom 3% of pixel values) in Matlab to enhance contrast.

2.3. Inline coherent imaging

The ICI system consists of a single-mode fiber-coupled, broadband superluminescent diode light source (BLM2D series, Superlum, 864 ± 37 nm), split into two free-space interferometer arms ("reference" and "sample", reference has fixed path length), and a high-speed spectrometer (see [57]). Compared to typical inline coherent imaging, the imaging beam is off-axis from the processing beam and exploits independent scanning and focusing optics. As shown in Fig. 1a, the sample arm of the interferometer was integrated into the BAMPRII environmental chamber and includes a MEMS scanner mirror (A5L2.2–7500 AU-TINY48.4-B/2TP, Mirrorcle Technologies, Inc.) for positioning and scanning the ICI beam, and a telecentric scanning lens (LSM05-BB, Thorlabs) and silver mirror for focusing and directing the imaging beam towards the sample and recollecting the backscattered imaging light. By aligning the ICI beam off-axis rather than coaxial to the laser beam, the sample arm could be integrated without changing the laser delivery optics (Fig. 1a). For fast computation, spectral interferograms recorded by the high-speed spectrometer are processed using a homodyne filtering technique similar to a fast Fourier transformation, as described by Webster *et al.* [58]. The system is characterized by an axial point spread function of 6 μm, measured experimentally and matching the theoretical value based on the bandwidth of the imaging light source [59], and a focused spot size (transverse resolution) of 35 μm.

2.4. Off-axis calibration

Though off-axis delivery allows completely independent imaging beam delivery and collection, care is needed to transform the topology measured with ICI into the frame of reference of the traverse and build directions (translation stage axes). Both the angle of incidence (AOI) of the imaging beam relative to the laser beam and the offset between the imaging and laser beam spots along the traverse axis need to be calibrated. The AOI of the imaging beam was measured to be (24 ± 1)° using a custom calibration plate (see Section 5.1). The offset between the imaging and laser beam spots was measured by spot welding a flat steel substrate at the laser and powder focal plane (nominal working distance from the nozzle where powder streams converge) and then measuring the morphology by scanning the imaging beam across the spot using the MEMS scanner mirror. Typical of laser spot welds, the edges of the marked spot were raised relative to the center and the virgin substrate and could easily be extracted from the ICI data for fitting and finding the centroid. The offset at this plane was calculated to be 1.36 mm. Knowing the angle of incidence, the offset for each ICI height measurement can then be calculated and ranged from ~1–1.75 mm (the higher the surface the larger the offset). This correction is included in the ICI data shown below.

2.5. Stability

To attribute the measured ICI height signature to actual changes in sample morphology, the temporal stability of the ICI system needs to be considered. Since ICI is an interferometric technique, motion on the order of half the center wavelength of the imaging light source over an integration time can reduce signal levels [60]. DED machines are typically highly noisy environments. To stabilize the interferometer, the ICI sample arm optics were mounted to the side wall of the BAMPRII enclosure and anchored with threaded metal rods to the ceiling to reduce cantilever effects. Since the sample holder was mounted onto the 3-axis stage (itself mounted to the floor of the enclosure), which includes both passive and active damping, any vibrations from the other BAMPRII subsystems could couple more easily into the ICI optics (through the frame and side wall) and would not be common with the sample.

To measure the temporal stability of the ICI system, ICI measurements were taken at 100 kHz over 100 ms and 10 kHz over 1 s. As discussed in ref. [57], an individual ICI measurement or "A-line" yields backscattered intensity as a function of height over the measurement range. Gaussian fitting of A-lines was then performed to extract centroid height over time with sub-pixel precision (as detailed in ref. [57]).

With a silver mirror tilted normal to the imaging beam AOI mounted in the sample holder and held stationary, single-point repeatability of ICI was measured to be 1.0 μm over 100 ms at 100 kHz and 1.02 μm over 1000 ms at 10 kHz (both 1 std. dev. in the measured height of a mirror over the imaging time). The longer timescale is on the same order as the single layer deposition times (between approx. 3 and 7 s). Although inter-layer dwell times are orders of magnitude larger, in situ ICI scans captured pre- and post-layer deposition can be used to recalibrate the ICI reference height.

The stability of the ICI beam position along the traverse axis was measured with a partially diffuse (sanded with 600 grit) Al plate, mounted flat to the sample holder and held stationary, and found to be 1.7 μm over 100 ms at 100 kHz and 3.0 μm over 1000 ms at 10 kHz (both 1 std. dev.).

To confirm that height changes measured with ICI were due primarily to shifts in the imaging beam position, the surface profile of the sanded Al plate was measured using focus variation microscopy (Keyence VHX). The surface roughness was found to be 0.15 μm (S_a), typical for metal surfaces sanded with 600 grit [61]. Any surface roughness will also be averaged over the imaging beam spot size of 35 μm, weighted by the intensity distribution. The height changes measured with ICI, which were on the order of ~1 μm, can then be attributed to shifts in the imaging beam position on the sample/along the traverse axis. The stability measurements were also taken at three different locations on the Al calibration plate to average over surface roughness. Finally, assuming a constant AOI, the change in measured ICI height relative to the initial value was converted to shifts in the traverse axis by dividing by the sine of the AOI. These deviations are sufficiently less than the axial point spread function (PSF) and imaging beam spot size of the ICI system (6 μm and 35 μm, respectively) to be ignored.

2.6. Synchronization with X-ray imaging

Finally, to synchronize ICI and synchrotron X-ray imaging, a trigger signal generated by BAMPRII was used to trigger both the laser and the Zebra box control system (Quantum Detectors) on the beamline, which then sent trigger signals to the MIRO 310M camera and ICI system. A programmable delay between the laser on time and synchrotron X-ray imaging and ICI was then used to delay imaging until the laser reached the seeded humps and valleys closer to the middle of the thin walls.

An example set of simultaneous, operando X-ray radiographs and ICI height signatures collected while depositing a layer of CM247LC on an IN718 substrate are shown in Fig. 1b-e. To generate an obvious change in height, the laser was intentionally switched off and on four separate times while depositing the track. ICI height data is overlaid on X-ray

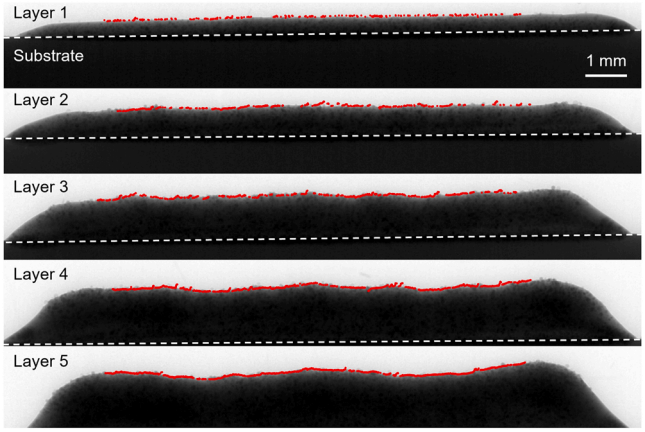

Fig. 2. Humping phenomena quantified in situ using ICI. Top surface profile measured operando using ICI (red data points) overlaid on corresponding synchrotron X-ray radiographs (stitched) for each layer of a five-layer thin-wall build. The two data sets are highly correlated, with correlation coefficients of 0.99, 0.97, 0.98, 0.93 and 0.98 (increasing layer number). Surface roughness (R_a) and surface waviness ($R_{a,\,w}$) were calculated from ICI data and found to be: 6, 10, 15, 14 and 13 μm, and 14, 16, 16, 31 and 47 μm (increasing layer number). Process parameters: laser power 200 W, traverse speed 2 mm/s, powder feedrate 3.4 g/min, substrate material IN718, powder material IN718 + 40 wt% WC.

radiographs from before, during and after the second off time (red dots in Fig. 1b-d), as well as stitched X-ray radiographs over the entire track (Fig. 1e). The high density of bright ICI measurements on the surface is attributed to (1) unlikelihood of occlusion by powder particles due to the short integration time of ICI (1.5 μs), and (2) the high dynamic range of ICI (>60 dB) capturing sufficient backscattered intensity from diffuse scatterers on the track surface. The top track profiles measured with ICI and radiography differ only at sintered powder particles, which are only sometimes centered on the track (Fig. 1d). ICI is more precise in measuring morphology within a narrow cross-section (here 35 μm), compared to radiography projections that include particles outside the center track. While the ICI imaging beam was held stationary to maximize the probability of capturing cracks and their morphology as detailed below, control of the MEMS scanner mirror (transverse scanning across the track surface) allows for imaging of the full 3D track morphology, limited only by the scanning speed of the mirror (approx. 1 m/s) relative to the traverse rate of the stage (see Appendix B).

3. Results and discussion

3.1. Humping phenomena

To quantify humping during a typical DED thin-wall build, the top surface profile was measured operando using ICI (Fig. 2). ICI data was downsampled by a factor of 100 from 0.04 μm traverse per ICI measurement to 4 μm using a weighted average with weights of ICI signal intensity. The data was also smoothed using a Gaussian filter one imaging beam spot size wide (30 μm). By transversely aligning the imaging beam with the processing laser as described in Section 3.3.1, the imaging beam is also well aligned to the center of the thin wall due to the Gaussian laser beam profile. The maximum build height also tends to fall along the center of the thin wall transversely, which was verified by transversely scanning the imaging beam (Appendix B) as well as ex situ sectioning and microscopy. This led to a high correlation between ICI and synchrotron X-ray imaging.

The top surface profile was broken down into surface roughness and waviness components using a standard Gaussian filter [62,63], with a cut-off wavelength λ_c of 2.0 mm. Surface roughness is mostly due to sintered powder particles, the number of which depends on the degree of pre-melting of incident particles through the powder flow rate and laser power [64]. Since these parameters are independent of the underlying geometry, it remains constant (within 1 std. dev.) after the first layer. By contrast, waviness, or humping in DED, was found to increase over the thin-wall build. This was confirmed ex situ with visual inspection and microscopy. Considering the AOI of the ICI imaging beam, this explains the relative sparsity of ICI data points in the first layer, which, due to its flatness and few sintered powder particles, more often leads to specular reflection of the imaging beam outside of the collection angle of the ICI optics rather than diffuse reflection. The high axial resolution of ICI allows for detection of surface waviness before it exceeds typical part tolerances (25–100 μm), creates stress concentrations and increases crack susceptibility.

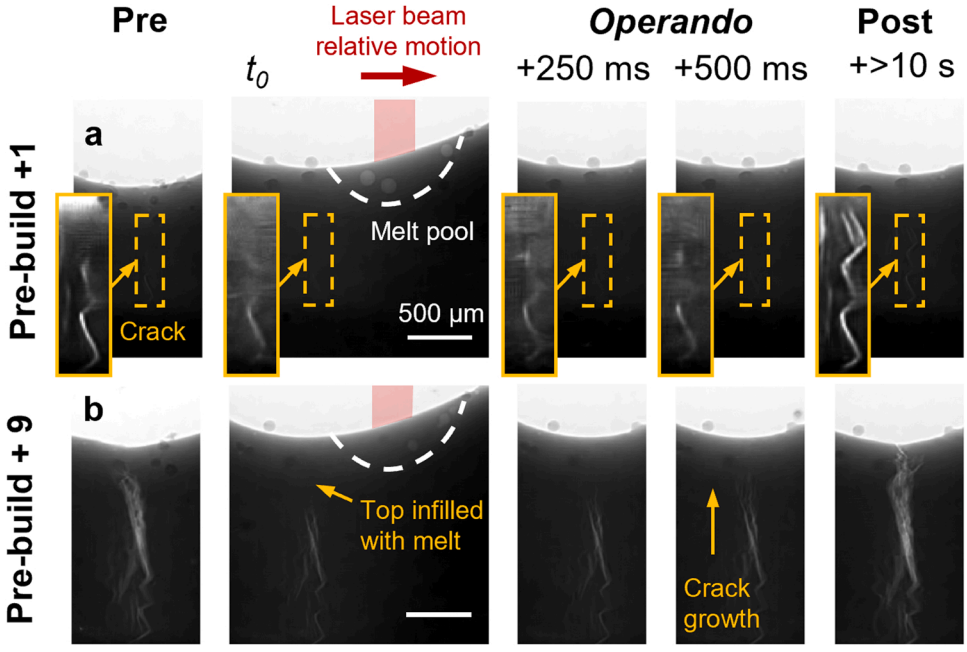

Fig. 3. Sub-surface crack infill and growth captured with operando X-ray imaging. Radiographs captured pre, during (operando) and post depositing layers 1 (a) and 9 (b) on a thin-wall pre-build. Typical of the prebuilds, a small crack (7 μm wide) is observable pre-deposition (a, pre). While depositing the first layer on the pre-build (Pre-build + 1), crack growth is only observable post-deposition (a, post). By layer 9 (Pre-build + 9), crack growth is observed 500 ms after the laser pass (b, operando), showing the decreasing time for cracks to grow and propagate to the surface with increasing residual stress. Insets are cropped around observed micro-crack (indicated by yellow arrow), scale 2:1. Radiographs are from the same valley. Process parameters: laser power 200 W, traverse speed 5 mm/s, powder feedrate 2.15 g/min, substrate material, pre-build and powder material: CM247LC. See Supplementary Movie 2 for full time-resolved observation of crack growth.

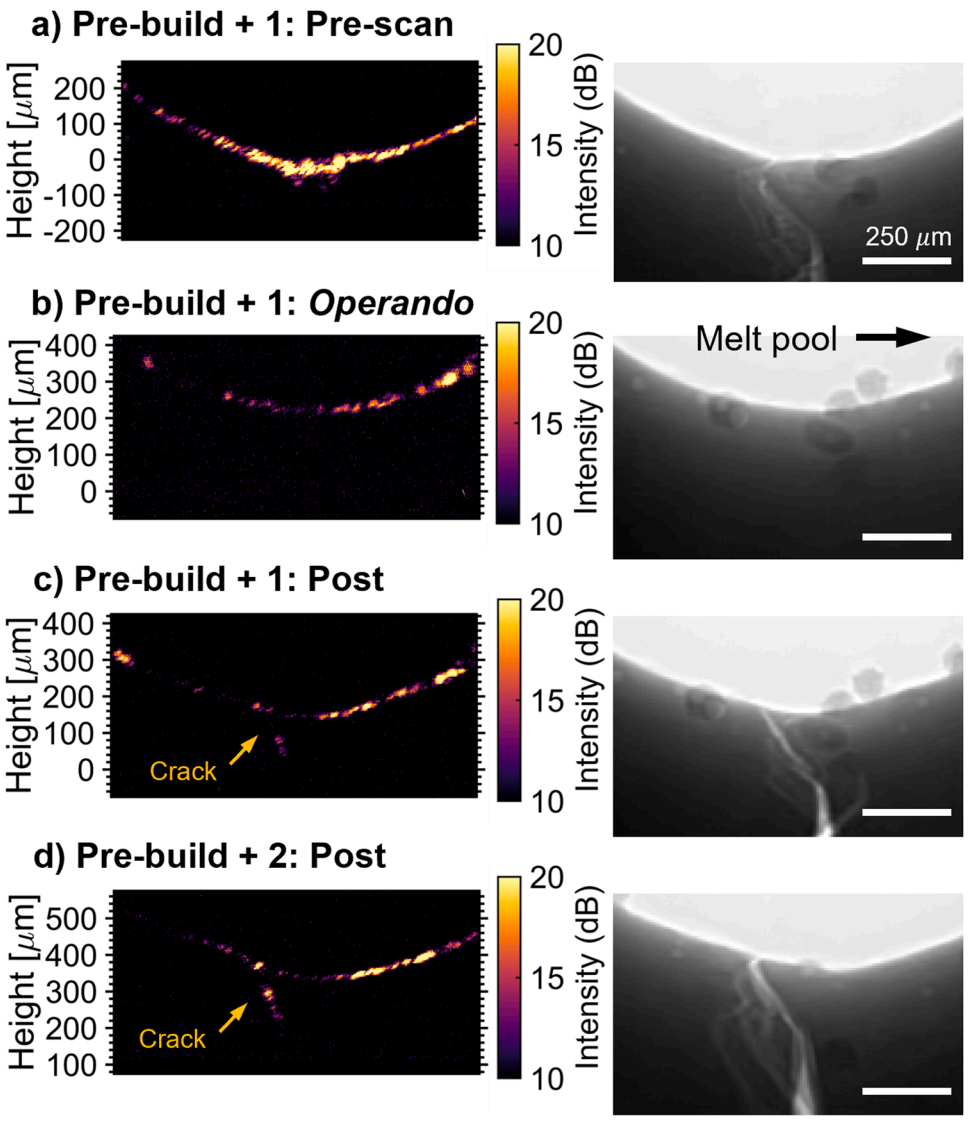

Fig. 4. Crack openings resolved in situ using ICI. ICI signatures and radiographs captured pre-processing (a), operando (b), and post-processing (c-d) over the 1st and 2nd layer built on a CM247LC thin-wall pre-build. The crack has reached the surface in (a) but with too small of an opening for ICI to fully resolve. By (c) and (d), the ICI signature includes clear sub-surface signal from the crack. Process parameters: laser power 200 W, traverse speed 2.5 mm/s, powder feedrate 2.15 g/min, substrate material,pre-build, powder material: CM247LC. ICI signatures and radiographs are to scale, with 250 μm scale bars.

3.2. Cracking

Here, we seed surface waviness into thin-wall builds to load the valleys with residual stress (see Appendix A). Similar to a Charpy V-notch test, cracking is then repeatably localized to the valleys and occurs within the next 5–10 layers deposited on the pre-built thin wall, allowing for imaging of cracking on the synchrotron beamline. The typical evolution over the layers deposited on the beamtime is shown in Fig. 3. Although the thin-wall pre-builds were built using the same process parameters, the valley depths were observed to differ by several 100 μm, leading to varying amounts of residual stress and cracking pre-beamtime.

Although none of the valleys in the pre-builds were initially entirely free of cracks, many had only one microcrack (<10 μm), like that shown in Fig. 3a. Radiographs captured pre, during (operando) and post depositing the first layer during the beamtime show a crack (yellow arrow) at the center of the valley. The crack is approximately 7 μm wide. The "lightning-bolt" or "zig-zag" shape matches the boundaries of a typical bi-directional AM grain morphology, related to epitaxial growth of columnar grains along the maximum thermal gradient, which alternates for the two laser traverse scanning directions [65]. As the laser beam passes over the valley during deposition, the top of the pre-existing crack interacts with the heat-affected zone (HAZ) and may be infilled with melt. This is difficult to resolve for the first layer due to the width of the crack (approx. equal to the X-ray imaging resolution) but is obvious for the ninth layer. The time t_0 is defined as the first frame when the tail of the melt pool passed the centerline of the crack. The same section of subsequent radiographs captured 250 ms and 500 ms after the laser pass and well after the valley has solidified ($\sim t_0 + 100$ ms) shows that the crack has grown back to the same size it was pre-deposition, but no further. However, the post-scan captured after the inter-layer dwell time of ~10 s shows significant growth of the crack towards the surface (from 450 ± 50 μm to 750 ± 50 μm measured in ImageJ). It also shows crack branching (two parallel sections closest to the surface). In the ninth layer (Pre-build + 9), crack growth is observed sooner after the laser beam passes and continues for approximately 500 ms. While no further growth was observed, the post-scan again shows that the crack has widened further and opened at the surface. Supplementary Movie 2 shows a progression of similar radiographs as Fig. 3a-b, but from a different pre-build with significant pre-existing cracks. Significantly faster crack growth is observed (approx. 2.5 mm/s from 100 to 200 ms after the laser pass operando vs. 0.6 mm/s from 250 to 500 ms operando Pre-build + 9 in Fig. 3), reaching one layer thickness below the surface after only 200 ms. The mechanism for crack formation as well as crack growth will be investigated in more detail in future work.

As mentioned above, neither new nor pre-existing cracks were

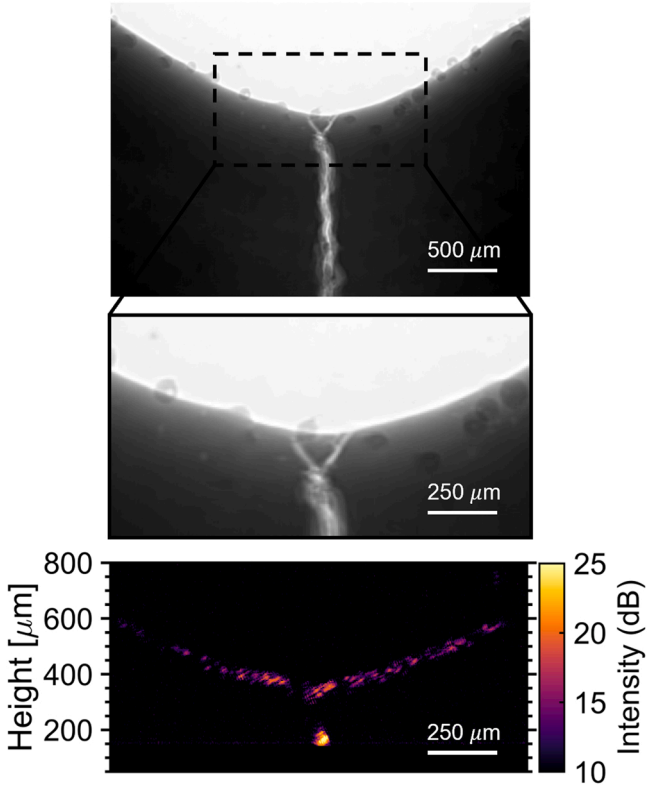

Fig. 5. Sub-surface ICI signal from a crack opening. Radiograph and ICI signature of a crack split at the track surface by a sintered powder particle, observed post-processing the 4th layer built on a CM247LC thin-wall pre-build. Process parameters: laser power 200 W, traverse speed 5 mm/s, 2.15 g/min, substrate material, pre-build, powder material: CM247LC.

observed to propagate to the track surface within the X-ray FOV time window (~3000 ms and ~1500 ms for traverse speeds of 2.5 mm/s and 5 mm/s). The ICI timing window for observing cracking was set by the offset between the ICI imaging beam and the high-power laser at the z-plane of the valley surface, which was held fixed for in situ and operando ICI measurements (no scanning with the MEMS). For the two traverse speeds used, 2.5 mm/s and 5 mm/s, this ranged from approximately 525 to 650 ms and 250–325 ms, depending on the position of the valley within the ICI measurement range. As this is shorter than the X-ray time window, crack openings were not measured with ICI operando. However, as with X-ray imaging, cracks were observed in situ with ICI during pre- and post-processing scans.

ICI measurements captured pre-, during and post-processing the first two layers deposited on a thin-wall build are shown below in Fig. 4, Fig. 5. Since the ICI signatures are from layers deposited on a pre-built, 2–3 mm tall thin wall, the substrate height is of less importance and ICI measurements have instead been referenced to the valley surface, which is set to 0 μm in the pre-scan before depositing the first layer. As shown in Fig. 4c-d, approximately 200 μm is then deposited within the valleys each layer. The deviation between the deposition height measured operando using ICI and the final deposition height after the thin wall has fully cooled to room temperature due to thermal contraction is expected to be < 10 μm (see Appendix B).

For most metallic surfaces, each ICI measurement or "A-line" (see Section 2.3) consists of a single peak in backscattered intensity at the height of the surface. This is due to the shallow penetration depth of infrared light in metals (<10 nm) [66]. The location of this peak can then be tracked over sequential A-lines to generate a signature of height over time, as in Fig. 1 and Fig. 2. However, for other morphologies, sufficient backscattered intensity can be collected from multiple interfaces. For example, a laser keyhole that is narrower than the imaging beam spot size can backscatter from both the substrate and the keyhole root. This is also true for crack openings at the valley surface. To show this, full A-lines are included in Fig. 4 rather than depth-tracked results, with color encoding backscatter light intensity relative to the noise floor of the ICI imaging system.

From the pre-scan before the first layer (Fig. 4a right), the radiograph shows a pre-existing crack in the valley with an opening that is at the resolution limit of the X-ray imaging system, a single pixel or less wide ($\leq$7 μm) and $>$ 5 times smaller than the ICI imaging beam spot size of 35 μm. Backscattered intensity is represented by the colorscale and is in log space as it varies over $>$ 3 orders of magnitude (from diffuse scatterers near the noise floor to specular reflectors near the saturation limit). Intensity is scaled relative to the standard deviation of the noise floor of the ICI system (meaning a value of 0 dB corresponds to a signal that matches the noise standard deviation after background subtraction). Considering the ICI signature from the pre-scan (Fig. 4a), higher intensity levels (>20 dB) were measured on the upslope (right) since this was close to normal with the imaging beam AOI. Oscillatory variations in intensity, more visible on the upslope but also present in the downslope, are caused by speckle, an inherent consequence of coherent imaging and a result of sub-ICI imaging resolution (<~ 7 μm) variations

	No. layers	z-increment (μm)
Beamtime	5	100
Pre-build	5	100
	4 (laser on/off)	50
	20	100

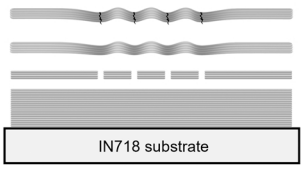

Fig. A2. Number of layers deposited in the pre-build and beamtime, including laser on/off layers in the pre-buid, for: laser power 200 W, traverse speed 5 mm/s, 2.15 g/min. Z-increments were chosen based on ICI height data from previous trials. Pre-build and beamtime layers were deposited using CM247LC powder, substrate used for pre-build was IN718.

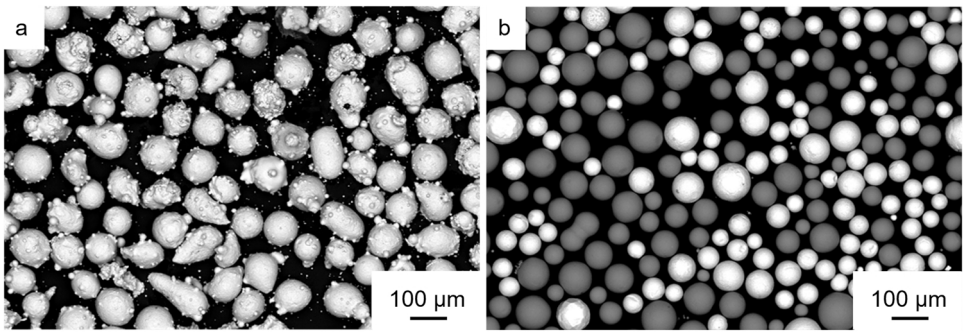

Fig. A1. Backscatter scanning electron image of (a) CM247LC and (b) IN718 + 40 wt% WC powders.

	No. layers	z-increment (μm)
Beamtime	5	250
Pre-build	5	250
	4 (laser on/off)	125
	10	250

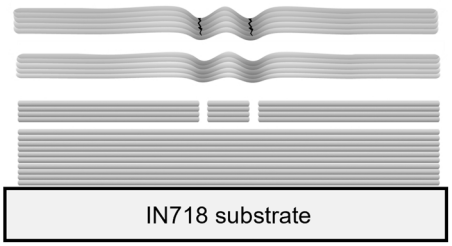

Fig. A3. Number of layers deposited in the pre-build and beamtime, including laser on/off layers in the pre-buid, for: laser power 200 W, traverse speed 2.5 mm/s, 2.15 g/min. Z-increments were chosen based on ICI height data from previous trials. Pre-build and beamtime layers were deposited using CM247LC powder, substrate used for pre-build was IN718.

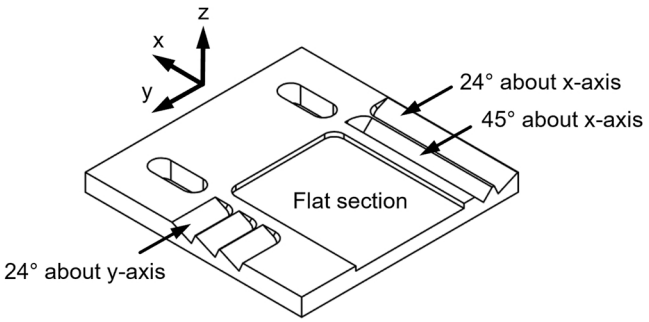

Fig. B1. Calibration plate used to calibrate the AOI of the ICI imaging beam, as well as measure the temporal stability of the ICI system along the stage traverse axis (y-axis). Frame of reference of the traverse and build directions (translation stage axes) is included in the upper left (xyz).

Table B1
Simulated temperature profile by layer number (from the top) and at the time of the operando ICI height measurement for calculating total deposition height.

Layer	Initial temperature (T_0) [K]
Top layer	1300
First from the top layer	1100
Second from the top layer	900
Third from the top layer	700
All other previously deposited layers (20 layers, pre-built thin wall was approx. 5 mm tall)	500

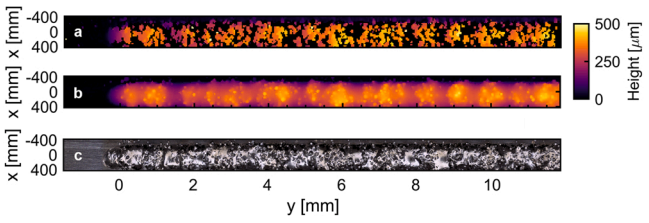

Fig. B2. Full 3D morphology of a single DED track measured (a) operando using ICI, (b) ex situ using focus variation microscopy and (c) visible light imaging (Bruker, Alicona InfiniteFocusG6). ICI profile was captured by scanning the imaging beam transversely using the MEMS scanner mirror (amplitude of 600 μm, frequency of 100 Hz) in addition to the motion of the traverse stage (4 mm/s). ICI data was downsampled into square pixels one imaging beam spot size wide ~30 μm. Process parameters: laser power 200 W, traverse speed 4 mm/s, 11.2 g/min, substrate material IN718, powder material IN718 + 70 wt % WC.

in the track surface within the imaging beam spot size [67]. These variations would also be smaller than the X-ray imaging pixel size, hence why the surface appears smooth in the radiograph. While two clusters of low-intensity, sub-surface ICI signal can be seen at the center of the valley near the location of the crack opening in the radiograph, they cannot be conclusively attributed to cracking, rather than an open pore for example, without X-ray imaging. Here sub-surface can be defined by the skin depth of the imaging (864 nm) and processing (1064 nm) beams, which is typically 1–10 nm for metals [66].

While the crack is partially infilled with melt during the laser pass (Fig. 4b right), the additional thermal and residual stresses from depositing subsequent layers then cause it to widen, from the initial 7 μm to 13–20 μm after the first layer (Fig. 4c right) to 27 μm after the second (Fig. 4d right). This is also evident in the corresponding ICI signatures, with increasing signal up to 150 μm below the valley surface. The source of backscattered intensity from within the crack is most likely diffuse scattering off of a combination of: (1) rough crack surfaces resulting from liquation cracking [68]; (2) intersections between adjacent sub-surface micro-cracks and the main crack, especially correlated with the clusters of ICI signal in the post-scan for the second layer; and (3) the change in crack orientation from ~30° to vertical (either due to the zig-zag morphology mentioned above or the sintered powder particles seen in the pre-scan) that occurs approximately 150 μm below the valley surface, the deepest measured ICI signal.

These sources of backscattered intensity were shared for most of the cracks observed with ICI. This is exemplified in Fig. 5 where a strong (approx. 25 dB) sub-surface signal intensity was recorded for a crack that branched near the surface and opened at two locations. In this case, the crack was oriented nearly parallel with the imaging beam, evident from the lack of signal along the sides of the crack. This highlights the benefit of delivering the ICI imaging beam off-axis. Grain orientation will change with thermal conditions, tending towards vertical with increasing traverse speed as well as colder underlying layers/substrate. Typical DED conditions produce orientations ranging from 0° to 45° relative to the build direction [69]. For these orientations, there is a higher probability that the imaging beam penetrates cracks and collects sufficient backscattered intensity within the crack for off-axis rather than inline delivery.

4. Conclusions

Operando, micron-scale and high-speed morphology measurements of the DED process using off-axis inline coherent imaging (ICI), coupled with simultaneous synchrotron X-ray radiography, revealed the causal link between humping and cracking in thin-walled structures of nickel super-alloy CM247LC.

Cracks were observed to form preferentially in lowered sections or valleys of thin walls with seeded humping, induced by locally increased residual stress. Each layer, X-ray imaging showed that the top section of

cracks was partially healed by the passing melt pool before re-opening, propagating towards the surface of the thin wall and, once sufficient residual stress built up, opening at the surface where they could be detected using ICI.

Crack widening and eventual opening at the surface was observed to extend over 1–10 s, well beyond the solidification time, highlighting the role of component-scale residual stress and the value of inter-layer defect detection. Driven by higher thermal gradients, much faster crack propagation and opening at the surface (<10 ms after laser beam passes) has been observed in PBF of CM247LC [52]. With an appropriate trailing offset, these crack openings should be observable operando with ICI, allowing for precise timing of crack propagation relative to the laser pass.

Humps of 250–500 μm in amplitude had to be seeded into thin-wall structures to induce cracking in the 10 layers deposited during a synchrotron beamtime. Sub-surface crack formation was not observed with X-ray imaging but likely occurred several layers before a crack opening at the surface. Due to its high axial resolution, ICI can detect humping of much smaller amplitude, well before it induces cracking. Cracking can then be reduced by controlling deposition height to prevent humping runaway.

CRediT authorship contribution statement

Tristan G. Fleming: Writing – review & editing, Writing – original draft, Project administration, Methodology, Investigation, Data curation, Conceptualization. **David Tien Rees:** Writing – review & editing, Methodology, Investigation, Conceptualization. **Sebastian Marussi:** Supervision, Methodology, Conceptualization. **Thomas Connolley:** Methodology, Investigation. **Robert C. Atwood:** Methodology, Investigation. **Martyn A. Jones:** Funding acquisition, Conceptualization. **James M. Fraser:** Writing – review & editing, Supervision, Project administration, Methodology, Funding acquisition, Conceptualization. **Chu Lun Alex Leung:** Writing – review & editing, Supervision, Methodology, Funding acquisition, Conceptualization. **D. Le Peter:** Supervision, Resources, Project administration, Methodology, Funding acquisition, Conceptualization, Writing – review & editing.

Declaration of competing interest

The authors declare the following financial interests/personal relationships which may be considered as potential competing interests: IPG Photonics (Canada) Inc. has commercialised inline coherent imaging. They are at arms-length to Queen's University. During the course of this work, authors were neither employees nor owners of this company.

Data availability

Data will be made available on request.

Acknowledgements

Research was performed using funding received from the Royal Academy of Engineering Chair in Emerging Technologies: Transforming Additive Manufacturing (CiET 1819/10).

PDL and CLAL are grateful for the support from MAPP: EPSRC Future Manufacturing Hub in Manufacture using Advanced Powder Processes (EP/P006566/1), EPSRC Impact Acceleration Account (EP/R511638/1), Manufacturing by Design (EP/W003333/1) and Made Smarter Innovation – Materials Made Smarter Research Centre (EP/V061798/1); CLAL is funded by Data-driven, Reliable, and Effective Additive Manufacturing using multi-BEAM technologies (EP/W037483/1).

TF and JMF acknowledge the support of the Natural Sciences and Engineering Research Council of Canada (NSERC), [funding reference number 5011063-2018], the NSERC Collaborative Research and Training Experience program [511093-2018], the Canadian Foundation for Innovation, and the Ontario Centres of Excellence.

The authors also acknowledge the use of facilities and support provided by the Research Complex at Harwell and thank the Diamond Light Source for providing the beamtime (MG28804–1) and the staff at JEEP-I12 beamline for technical assistance. Many thanks to the team members from the Materials, Structure and Manufacturing group at Harwell (MSM@H) for their assistance in preparation for and during the beamtime: Dr. Yuze Huang and Xianqiang Fan. An additional thank you to Dr. Ranveer Matharu, Coventry University for his help with ex situ focus variation microscopy.

Appendix A. : Directed energy deposition

Powder characterization

See Figs. A1-A3.

Pre-build strategy with seeded humping

To ensure cracking was captured with X-ray imaging and ICI, thin walls seeded with humping were pre-built and used as substrates for layers deposited on the beamtime. Humping was seeded by turning the laser on/off while depositing four of the layers during the pre-build, as depicted in Figure A2 and Figure A3. Only two valleys (one hump) were seeded into pre-builds built with a traverse speed of 2.5 mm/s, compared to four valleys (three humps) for a traverse speed of 5 mm/s. This was chosen such that all valleys could be imaged during the maximum X-ray imaging time of 5000 ms for the chosen field of view and acquisition rate of 1 kHz, dictated by the onboard memory of the MIRO 310 M camera. As described in Section 4, seeded humping concentrated residual stress to the valleys and localized cracking. The number of layers included in the pre-build was adjusted to maximize the likelihood that cracking occurred in the 5–10 layers deposited during the synchrotron beamtime. This resulted in a different strategy for traverse speeds of 2.5 mm/s and 5 mm/s.

Appendix B. : Inline coherent imaging

ICI angle of incidence calibration

The calibration plate (50×50×4 mm) used to calibrate the AOI of the ICI imaging beam relative to the laser beam is shown in Fig. B1 below. The plate was machined out of aluminum alloy 6061. The flat and angled surfaces were then sanded with 600-grit sandpaper. The plate was mounted directly onto and aligned with the BAMPRII translation stages (*xyz* frame of reference).

The calibration procedure benefits greatly from the use of a telecentric scanning lens (Thorlabs LSM05-BB), which ensured a constant AOI regardless of the angle of the MEMS scanner mirror (Fig. 1). For all measurements, the MEMS mirror was scanned in a sinusoidal pattern at a frequency of 100 Hz and ICI measurements were captured at 100 kHz. The amplitude of the sinusoidal voltage pattern applied to the MEMS scanner mirror was held constant and dictated the distance the imaging beam was scanned along the y-axis, which was also unknown before calibration.

The alignment of the MEMS scanner axis with the *x* and *y* axes was first confirmed by scanning the imaging beam along the section angled at 24°

about the x-axis and rotating the MEMS mirror until no height change was observed using ICI during the scan. To measure the AOI (in the *y-z* plane), the imaging beam was scanned along the y-axis on both the flat section as well as the angled sections machined to be 24° about the x-axis and 45° about the x-axis. The angles of these surfaces represented the "knowns" in the calibration procedure, the AOI and scanning distance for a given voltage applied to the MEMS being the "unknowns". By measuring the resulting changes in height along the imaging beam axis for each section, the two "unknowns" could be calculated using any pair of height datasets for the three sections. Having an additional "known" allowed for improved precision.

Error due to thermal expansion/contraction

Calculating final deposition height as the difference between substrate height measured with ICI pre-deposition and ICI height data collected in situ requires some consideration of thermal expansion/contraction of the deposit. To minimize the total build time in an industrial DED machine, ICI height data would ideally be collected operando rather than in situ inter-layer. We then want to calculate the expected thermal contraction of a thin wall from when the ICI measurement is taken operando to after it has been allowed to fully cool to room temperature (RT).

Due to the high cooling rates in DED and the offset of the ICI beam from the laser beam (1.36 mm here, approx. 540 ms at 2.5 mm/s traverse speed and 270 ms at 5 mm/s), the layer being deposited will have already cooled from the liquidus temperature by several hundred K (cooling rates immediately after the laser pass >1000 K/s) when the operando ICI measurement is taken. Based on $T_{liq} = 1641K$ for CM247LC [70], we assume a change in temperature ΔT of 1000 K for the top layer Table B1.

Here, we included significant dwell times (>10 s) for inter-layer X-ray and ICI imaging, which allowed the thin wall to cool significantly. During industrial DED, the inter-layer dwell time would be minimized to maximize build efficiency. Previously deposited layers are then expected to remain at elevated temperatures throughout the build. This is in addition to the rapid temperature increases in the layers closest to the top [24]. To simplify the thermal contraction calculation, we assume the following starting temperature profile with layer number:

With this starting temperature profile, and assuming a layer thickness of 250 μm matching the 2.5 mm/s thin-wall builds we can calculate the thermal contraction of each layer according to:

$$\Delta h = h_0 \cdot \alpha \cdot \Delta T$$

where Δh is the change in deposit height, h_0 is the original deposit height (in situ), α is the coefficient of linear thermal expansion, and ΔT is the temperature change. Substituting values of $h_0 = 250\mu m$, $\alpha = 1.8 \times 10^{-5}\ \ K^{-1}$, $\Delta T = 200 - 1000K$, we find that the deposit will contract by $\Delta h \approx 30\mu m$. Although this is a highly simplified model, it is only used as an upper estimate of the error in ICI layer thickness measurements due to thermal expansion/contraction.

While this corresponds to a relative uncertainty in final deposit height of only 0.5% (30 μm over 6 mm), it can be further reduced by calculating the thickness of each deposited layer as the difference between subsequent operando height measurements. The final deposit height could then be calculated by summing over the values for layer thickness. This removes any thermal contraction common to subsequent height measurements, at least any slow heat build-up. Removing the thermal contraction of all layers aside from the top four, the error due to thermal contraction is reduced to $\Delta h \approx 10\mu m$.

ICI transverse scanning

The full 3D morphology of a single track measured operando with ICI is shown below in Figure B2a. As a result of the chosen scanning amplitude of the MEMS scanner, only one of the edges of the track (approx. x = −300 μm) is visible. Dark (black) sections within the track were below the noise floor of the ICI imaging system. This is due to specular reflection of the imaging light outside of the collection angle of the ICI optics. To better understand the sources of backscattered intensity from the track surface, the track was imaged ex situ using focus variation microscopy and visible light imaging (Fig. B2b and c).

A clear balling morphology can be seen in both ex situ images, with larger numbers of sintered powder particles on the raised areas. This can be attributed to the high powder flow rate (11.2 g/min) and the ratio of blended WC particles (70 wt%) used to deposit the track, which can lead to unstable powder delivery. Without sintered powder particles to diffusely scatter the ICI imaging light, lowered areas are more often dark. The exceptions are surfaces close to perpendicular with the ICI imaging beam, at approximately y = 0 mm (beginning of the track) and y = 1.75 mm for example.

Appendix C. Supporting information

Supplementary data associated with this article can be found in the online version at doi:10.1016/j.addma.2023.103579.

References

[1] ISO/ASTM, 52900 - Additive Manufacturing - General principles - Fundamentals and vocabulary (2nd ed.), , 2021 28. ⟨www.iso.orgwww.astm.org⟩.

[2] J.E. Smugeresky, D.M. Keicher, J.A. Romero, M.L. Griffith, L.D. Harwell, Laser engineered net shaping (LENS) for fabrication of metallic components, Albuquerque, NM, and Livermore, CA (U. S.) (1996), https://doi.org/10.2172/554828.

[3] G. Piscopo, L. Iuliano, Current research and industrial application of laser powder directed energy deposition, Int. J. Adv. Manuf. Technol. 119 (2022) 6893–6917, https://doi.org/10.1007/S00170-021-08596-W.

[4] A.M. Khorasani, I. Gibson, J.K. Veetil, A.H. Ghasemi, A review of technological improvements in laser-based powder bed fusion of metal printers, Int. J. Adv. Manuf. Technol. 108 (2020) 191–209, https://doi.org/10.1007/S00170-020-05361-3/TABLES/15.

[5] M. Ansari, E. Jabari, E. Toyserkani, Opportunities and challenges in additive manufacturing of functionally graded metallic materials via powder-fed laser directed energy deposition: a review, J. Mater. Process. Technol. 294 (2021), 117117, https://doi.org/10.1016/J.JMATPROTEC.2021.117117.

[6] D. Svetlizky, M. Das, B. Zheng, A.L. Vyatskikh, S. Bose, A. Bandyopadhyay, J. M. Schoenung, E.J. Lavernia, N. Eliaz, Directed energy deposition (DED) additive manufacturing: physical characteristics, defects, challenges and applications, Mater. Today 49 (2021) 271–295, https://doi.org/10.1016/J.MATTOD.2021.03.020.

[7] M.J. Donachie, S.J. Donachie, Superalloys: A technical guide, 2nd ed., ASM International, Materials Park, Ohio, 2002.

[8] P.A. McNutt, An investigation of cracking in laser metal deposited nickel superalloy CM247LC. EngD Thesis, University of Birmingham,, 2015. ⟨https://etheses.bham.ac.uk/id/eprint/6394/⟩.

[9] L.M. Amoo, On the design and structural analysis of jet engine fan blade structures, Prog. Aerosp. Sci. 60 (2013) 1–11, https://doi.org/10.1016/J.PAEROSCI.2012.08.002.

[10] L. Zhu, N. Li, P.R.N. Childs, Light-weighting in aerospace component and system design, Propuls. Power Res 7 (2018) 103–119, https://doi.org/10.1016/J.JPPR.2018.04.001.

[11] J. Plocher, A. Panesar, Review on design and structural optimisation in additive manufacturing: towards next-generation lightweight structures, Mater. Des. 183 (2019), 108164, https://doi.org/10.1016/J.MATDES.2019.108164.

[12] D. Olvera, A. Calleja, L.N. López de Lacalle, F. Campa, A. Lamikiz, Flank milling of complex surfaces, in: Mach. Complex Sculpt. Surfaces, Springer, London, 2012, pp. 1–31, https://doi.org/10.1007/978-1-4471-2356-9_1.

[13] S. Herranz, F.J. Campa, L.N.L. De Lacalle, A. Rivero, A. Lamikiz, E. Ukar, J. A. Sánchez, U. Bravo, The milling of airframe components with low rigidity: a general approach to avoid static and dynamic problems, J. Eng. Manuf. 219 (2005) 789–801, https://doi.org/10.1243/095440505×32742.
[14] G. Wu, W. Pan, X. Wang, J. Mo, S. Ding, Chatter and deformation in machining thin-walled flexible components, IOP Conf. Ser. Mater. Sci. Eng. 423 (2018), 012035, https://doi.org/10.1088/1757-899X/423/1/012035.
[15] A. Gasser, G. Backes, I. Kelbassa, A. Weisheit, K. Wissenbach, Laser metal deposition (LMD) and selective laser melting (SLM) in turbo-engine applications, Laser Tech. J. 7 (2010) 58–63, https://doi.org/10.1002/LATJ.201090029.
[16] M.K. Keshavarz, A. Gontcharov, P. Lowden, A. Chan, D. Kulkarni, M. Brochu, Turbine blade tip repair by laser directed energy deposition additive manufacturing using a Rene 142–MERL 72 powder blend, J. Manuf. Mater. Process 5 (2021) 21, https://doi.org/10.3390/JMMP5010021.
[17] C.D. Jamieson, M.C. Brennan, T.J. Spurgeon, S.W. Brown, J.S. Keist, E.W. Reutzel, Tailoring alloy 718 laser directed energy deposition process strategies for repair applications, J. Laser Appl. 34 (2022), 012018, https://doi.org/10.2351/7.0000534.
[18] H.L. Wei, T. Mukherjee, W. Zhang, J.S. Zuback, G.L. Knapp, A. De, T. DebRoy, Mechanistic models for additive manufacturing of metallic components, Prog. Mater. Sci. 116 (2021), 100703, https://doi.org/10.1016/J.PMATSCI.2020.100703.
[19] V. Luzin, N. Hoye, Stress in thin wall structures made by layer additive manufacturing, Mater. Res. Proc. 2 (2017) 497–502, https://doi.org/10.21741/9781945291173-84.
[20] B. Blakey-Milner, P. Gradl, G. Snedden, M. Brooks, J. Pitot, E. Lopez, M. Leary, F. Berto, A. du Plessis, Metal additive manufacturing in aerospace: a review, Mater. Des. 209 (2021), 110008, https://doi.org/10.1016/J.MATDES.2021.110008.
[21] M. Izadi, A. Farzaneh, M. Mohammed, I. Gibson, B. Rolfe, A review of laser engineered net shaping (LENS) build and process parameters of metallic parts, Rapid Prototyp. J. 26 (2020) 1059–1078, https://doi.org/10.1108/RPJ-04-2018-0088/FULL/PDF.
[22] A.J. Pinkerton, L. Li, The significance of deposition point standoff variations in multiple-layer coaxial laser cladding (coaxial cladding standoff effects), Int. J. Mach. Tools Manuf. 44 (2004) 573–584, https://doi.org/10.1016/J.IJMACHTOOLS.2004.01.001.
[23] B. Bax, R. Rajput, R. Kellet, M. Reisacher, Systematic evaluation of process parameter maps for laser cladding and directed energy deposition, Addit. Manuf. 21 (2018) 487–494, https://doi.org/10.1016/J.ADDMA.2018.04.002.
[24] V. Manvatkar, A. De, T. DebRoy, Spatial variation of melt pool geometry, peak temperature and solidification parameters during laser assisted additive manufacturing process, Mater. Sci. Technol. 31 (2015) 924–930, https://doi.org/10.1179/1743284714Y.0000000701.
[25] M. Liu, A. Kumar, S. Bukkapatnam, M. Kuttolamadom, A review of the anomalies in directed energy deposition (DED) processes & potential solutions - part quality & defects, Procedia Manuf. 53 (2021) 507–518, https://doi.org/10.1016/J.PROMFG.2021.06.093.
[26] J.C. Haley, B. Zheng, U.S. Bertoli, A.D. Dupuy, J.M. Schoenung, E.J. Lavernia, Working distance passive stability in laser directed energy deposition additive manufacturing, Mater. Des. 161 (2019) 86–94, https://doi.org/10.1016/J.MATDES.2018.11.021.
[27] R.C. Reed, The Superalloys: Fundamentals and Applications, Cambridge University Press, Cambridge, 2006.
[28] Z. Zhou, L. Huang, Y. Shang, Y. Li, L. Jiang, Q. Lei, Causes analysis on cracks in nickel-based single crystal superalloy fabricated by laser powder deposition additive manufacturing, Mater. Des. 160 (2018) 1238–1249, https://doi.org/10.1016/J.MATDES.2018.10.042.
[29] E. Chauvet, P. Kontis, E.A. Jägle, B. Gault, D. Raabe, C. Tassin, J.J. Blandin, R. Dendievel, B. Vayre, S. Abed, G. Martin, Hot cracking mechanism affecting a non-weldable Ni-based superalloy produced by selective electron Beam Melting, Acta Mater. 142 (2018) 82–94, https://doi.org/10.1016/J.ACTAMAT.2017.09.047.
[30] X. Lu, X. Lin, M. Chiumenti, M. Cervera, Y. Hu, X. Ji, L. Ma, H. Yang, W. Huang, Residual stress and distortion of rectangular and S-shaped Ti-6Al-4V parts by directed energy deposition: modelling and experimental calibration, Addit. Manuf. 26 (2019) 166–179, https://doi.org/10.1016/j.addma.2019.02.001.
[31] H. Wang, W. Liu, Z. Tang, Y. Wang, X. Mei, K.M. Saleheen, Z. Wang, H. Zhang, Review on adaptive control of laser-directed energy deposition, Opt. Eng. 59 (2020), 070901, https://doi.org/10.1117/1.OE.59.7.070901.
[32] S.K. Everton, M. Hirsch, P. Stravroulakis, R.K. Leach, A.T. Clare, Review of in-situ process monitoring and in-situ metrology for metal additive manufacturing, Mat. Des. 95 (2016) 431–445, https://doi.org/10.1016/j.matdes.2016.01.099.
[33] Y. AbouelNour, N. Gupta, In-situ monitoring of sub-surface and internal defects in additive manufacturing: a review, Mat. Des. 222 (2022), 111063, https://doi.org/10.1016/j.matdes.2022.111063.
[34] Z. Tang, W. Liu, Y. Wang, K.M. Saleheen, Z. Liu, S. Peng, Z. Zhang, H. Zhang, A review on in situ monitoring technology for directed energy deposition of metals, Int. J. Adv. Manuf. Tech. 108 (2020) 3437–3463, https://doi.org/10.1007/s00170-020-05569-3.
[35] T.L. Starr, In-line process monitoring of powder-bed fusion and directed-energy deposition processes, in: D.L. Bourell, W. Frazier, H. Kuhn, M. Seifi (Eds.), ASM Handbook Volume 24: Additive manufacturing processes, ASM International, 2020, pp. 287–297, https://doi.org/10.31399/ASM.HB.V24.A0006564.
[36] N. Sridharan, J.S. Baba, B.H. Jordan, R.B. Dinwiddie, R.R. Dehoff, Understanding part to part variability during directed energy deposition processes using in situ and ex situ process characterization, Oak Ridge, TN (U. S.) (2018), https://doi.org/10.2172/1459280.
[37] L. Chen, X. Yao, P. Xu, S.K. Moon, G. Bi, Rapid surface defect identification for additive manufacturing with in-situ point cloud processing and machine learning, Virtual Phys. Prototyp. 16 (2020) 50–67, https://doi.org/10.1080/17452759.2020.1832695.
[38] J.C. Heigel, P. Michaleris, T.A. Palmer, In situ monitoring and characterization of distortion during laser cladding of Inconel® 625, J. Mater. Process. Technol. 220 (2015) 135–145, https://doi.org/10.1016/J.JMATPROTEC.2014.12.029.
[39] I. Garmendia, J. Leunda, J. Pujana, A. Lamikiz, In-process height control during laser metal deposition based on structured light 3D scanning, Procedia CIRP 68 (2018) 375–380, https://doi.org/10.1016/J.PROCIR.2017.12.098.
[40] E. Toyserkani, A. Khajepour, A mechatronics approach to laser powder deposition process, Mechatronics 16 (2006) 631–641, https://doi.org/10.1016/J.MECHATRONICS.2006.05.002.
[41] M. Biegler, B. Graf, M. Rethmeier, In-situ distortions in LMD additive manufacturing walls can be measured with digital image correlation and predicted using numerical simulations, Addit. Manuf. 20 (2018) 101–110, https://doi.org/10.1016/J.ADDMA.2017.12.007.
[42] B. Jordan, C. Leach, J. Haley, R. Dehoff, V. Paquit, In-situ digital image correlation and thermal monitoring in directed energy deposition additive manufacturing, Opt. Express 29 (2021) 9927–9941, https://doi.org/10.1364/OE.416659.
[43] S. Donadello, M. Motta, A.G. Demir, B. Previtali, Monitoring of laser metal deposition height by means of coaxial laser triangulation, Opt. Lasers Eng. 112 (2019) 136–144, https://doi.org/10.1016/J.OPTLASENG.2018.09.012.
[44] D. Markus Kogel-Hollacher, M. Strebel, C. Staudenmaier, H.-I. Schneider, D. Regulin, M. Kogel-Hollacher, OCT sensor for layer height control in DED using SINUMERIK® controller, Laser 3D Manuf. VII 11271 (2020) 59–63, https://doi.org/10.1117/12.2540167.
[45] L.W. Koester, H. Taheri, T.A. Bigelow, L.J. Bond, E.J. Faierson, In-situ acoustic signature monitoring in additive manufacturing processes, AIP Conf. Proc. 1949 (2018), 020006, https://doi.org/10.1063/1.5031503.
[46] H. Taheri, L.W. Koester, T.A. Bigelow, E.J. Faierson, L.J. Bond, In situ additive manufacturing process monitoring with an acoustic technique: clustering performance evaluation using k-means algorithm, J. Manuf. Sci. Eng. 141 (2019), 041011, https://doi.org/10.1115/1.4042786.
[47] H. Gaja, F. Liou, Defect classification of laser metal deposition using logistic regression and artificial neural networks for pattern recognition, Int. J. Adv. Manuf. Technol. 94 (2018) 315–326, https://doi.org/10.1007/s00170-017-0878-9.
[48] T. Hauser, R.T. Reisch, T. Kamps, A.F.H. Kaplan, J. Volpp, Acoustic emissions in directed energy deposition processes, Int. J. Adv. Manuf. Technol. 119 (2022) 3517–3532, https://doi.org/10.1007/S00170-021-08598-8.
[49] P.J.L. Webster, L.G. Wright, Y. Ji, C.M. Galbraith, A.W. Kinross, C. Van Vlack, J. M. Fraser, Automatic laser welding and milling with in situ inline coherent imaging, Opt. Lett. 39 (2014) 6217, https://doi.org/10.1364/OL.39.006217.
[50] S.M.H. Hojjatzadeh, N.D. Parab, Q. Guo, M. Qu, L. Xiong, C. Zhao, L.I. Escano, K. Fezzaa, W. Everhart, T. Sun, L. Chen, Direct observation of pore formation mechanisms during LPBF additive manufacturing process and high energy density laser welding, Int. J. Mach. Tools Manuf. 153 (2020), 103555, https://doi.org/10.1016/j.ijmachtools.2020.103555.
[51] N. Kouraytem, P.J. Chiang, R. Jiang, C. Kantzos, J. Pauza, R. Cunningham, Z. Wu, G. Tang, N. Parab, C. Zhao, K. Fezzaa, T. Sun, A.D. Rollett, Solidification crack propagation and morphology dependence on processing parameters in AA6061 from ultra-high-speed x-ray visualization, Addit. Manuf. 42 (2021), 101959, https://doi.org/10.1016/J.ADDMA.2021.101959.
[52] H. Ghasemi-Tabasi, C. de Formanoir, S. Van Petegem, J. Jhabvala, S. Hocine, E. Boillat, N. Sohrabi, F. Marone, D. Grolimund, H. Van Swygenhoven, R.E. Logé, Direct observation of crack formation mechanisms with operando laser powder bed fusion X-ray imaging, Addit. Manuf. 51 (2022), 102619, https://doi.org/10.1016/J.ADDMA.2022.102619.
[53] Y. Chen, S.J. Clark, L. Sinclair, C.L.A. Leung, S. Marussi, T. Connolley, O. V. Magdysyuk, R.C. Atwood, G.J. Baxter, M.A. Jones, D.G. McCartney, I. Todd, P. D. Lee, In situ and operando x-ray imaging of directed energy deposition additive manufacturing (arXiv), arXiv 2006 (2020) 09087, https://doi.org/10.48550/arxiv.2006.09087.
[54] C. Lun, A. Leung, S. Marussi, R.C. Atwood, M. Towrie, P.J. Withers, P.D. Lee, In situ X-ray imaging of defect and molten pool dynamics in laser additive manufacturing, Nat. Commun. 9 (2018) 1355, https://doi.org/10.1038/s41467-018-03734-7.
[55] I. The Mathworks, 2-D Gaussian filtering of images - MATLAB imgaussfilt, (n.d.). ⟨https://www.mathworks.com/help/images/ref/imgaussfilt.html⟩ (accessed June 23, 2022).
[56] M. Maggioni, G. Boracchi, A. Foi, K. Egiazarian, Video denoising, deblocking, and enhancement through separable 4-D nonlocal spatiotemporal transforms, IEEE Trans. Image Process 21 (2012) 3952–3966, https://doi.org/10.1109/TIP.2012.2199324.
[57] J.A. Kanko, A.P. Sibley, J.M. Fraser, In situ morphology-based defect detection of selective laser melting through inline coherent imaging, J. Mater. Process. Technol. 231 (2016) 488–500, https://doi.org/10.1016/j.jmatprotec.2015.12.024.
[58] P.J.L. Webster, L.G. Wright, K.D. Mortimer, B.Y. Leung, J.X.Z. Yu, J.M. Fraser, Automatic real-time guidance of laser machining with inline coherent imaging, J. Laser Appl. 23 (2011), 022001, https://doi.org/10.2351/1.3567955.
[59] W. Drexler, J.G. Fujimoto, Optical Coherence Tomography, Springer Berlin Heidelberg, Berlin, Heidelberg, 2008.

[60] S.H. Yun, G.J. Tearney, J.F. de Boer, B.E. Bouma, Motion artifacts in optical coherence tomography with frequency-domain ranging, Opt. Express 12 (2004) 2977, https://doi.org/10.1364/OPEX.12.002977.
[61] The European Stainless Steel Development Association, Roughness measurements of stainless steel surfaces, Brussels, 2014.
[62] ASME, B46.1 - 2019 Surface Texture (Surface Roughness, Waviness, and Lay), 2020.
[63] ISO, ISO 16610–21:2011 Geometric product specifications (GPS) - Filtration - Part 21: Linear profile filters: Gaussian filters, 2011.
[64] M. Gharbi, P. Peyre, C. Gorny, M. Carin, S. Morville, P. Le Masson, D. Carron, R. Fabbro, Influence of various process conditions on surface finishes induced by the direct metal deposition laser technique on a Ti–6Al–4V alloy, J. Mater. Process. Technol. 213 (2013) 791–800, https://doi.org/10.1016/J.JMATPROTEC.2012.11.015.
[65] L. Thijs, F. Verhaeghe, T. Craeghs, J. Van Humbeeck, J.P. Kruth, A study of the microstructural evolution during selective laser melting of Ti-6Al-4V, Acta Mater. 58 (2010) 3303–3312, https://doi.org/10.1016/j.actamat.2010.02.004.
[66] E.D. Palik, Handbook of Optical Constants of Solids, 5th ed., Academic Press Elsevier Inc., College Park, Maryland, 1997.
[67] A. Curatolo, B.F. Kennedy, D.D. Sampson, T.R. Hillman, Speckle in optical coherence tomography, J. Biomed. Opt. 4 (1999) 95–105, https://doi.org/10.1117/1.429925.
[68] J.C. Lippold, S.D. Kiser, J.N. DuPont, Welding Metallurgy and Weldability of Nickel-Base Alloys, Wiley, Hoboken, New Jersey, 2009.
[69] G.P. Dinda, A.K. Dasgupta, J. Mazumder, Laser aided direct metal deposition of Inconel 625 superalloy: microstructural evolution and thermal stability, Mater. Sci. Eng. A 509 (2009) 98–104, https://doi.org/10.1016/j.msea.2009.01.009.
[70] H.C. Basoalto, C. Panwisawas, Y. Sovani, M.J. Anderson, R.P. Turner, B. Saunders, J.W. Brooks, A computational study on the three-dimensional printability of precipitate-strengthened nickel-based superalloys, Proc. R. Soc. A 474 (2018), https://doi.org/10.1098/RSPA.2018.0295.